Thermal Science and Engineering Progress 75 (2026) 104770

Contents lists available at ScienceDirect

Thermal Science and Engineering Progress

journal homepage: www.elsevier.com/locate/tsep

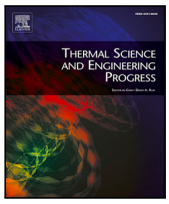

Thermodynamic consistent modeling of flame–solid interaction and thermo-mechanical response of high-temperature materials

Chunkan Yu [a,*], Frederik Hille [b], Thomas Böhlke [b], Michael Fischlschweiger [a]

[a] Institute of Technical Thermodynamics, Karlsruhe Institute of Technology (KIT), Engelbert-Arnold-Str. 4, Karlsruhe, 76131, Germany
[b] Institute of Engineering Mechanics, Karlsruhe Institute of Technology (KIT), Kaiserstraße 10, Karlsruhe, 76131, Germany

ARTICLE INFO

Keywords:
Laminar premixed flame
Ammonia/hydrogen
Gough-Joule effect
Quasi-static assumption
Flame–solid interaction

ABSTRACT

A fully coupled flame–solid interaction problem is investigated using a laminar strained premixed ammonia/hydrogen/air flame stabilized at a plane wall. Heat transfer from the flame to the wall is explicitly considered, and the resulting transient temperature evolution within the solid leads to combustion-induced deformation and stress development. Inconel 718 is selected as a representative wall material, and its temperature-dependent thermo-physical properties are described using thermodynamically consistent formulations derived from the Helmholtz energy. It can be shown, that a linear temperature dependency for the bulk and shear modulus, as well as for the thermal expansion coefficient directly implies a strain dependency of the heat capacity at constant strain. This contribution to the heat capacity turns out to be negligible for the here investigated Inconel 718. Both steady-state and transient configurations are examined. In the steady-state configuration, the influence of thermal radiation on the temperature distribution inside the plane wall is assessed. In the transient configuration, a cold plane wall is suddenly introduced into the flame system and subsequently heated, and the entire heating process is investigated under varying imposed flame strain rates. The results show that increasing flame strain rate accelerates wall heating and shortens the time required for thermo-mechanical stress to reach the material yield strength, despite reduced flame temperatures. The quasi-static assumption for the balance equation of linear momentum is validated, while the Gough–Joule effect is shown to be negligible for the conditions considered. These findings provide fundamental insight into transient flame-induced heating and thermo-mechanical response of solid structures.

1. Introduction

Understanding the interaction between combustion processes and the corresponding material behavior is fundamental to advancing process safety, energy efficiency and high-temperature material design. During combustion, materials undergo complex thermo-chemo-mechanical loading such as corrosion [1,2], phase change [3,4] and structural damage [5,6]. Therefore, such coupled flame–solid interaction processes are recognized as a critical role in determining the overall stability and efficiency of combustion systems, as well as the thermal performance and failure modes of engineering materials exposed to high-temperature environments. For steady premixed strained flames, pressure-induced enhancement of interfacial temperature gradients has been shown to significantly increase thermo-mechanical loading on solid material, with stresses reaching or exceeding the yield strength [7]. Related studies on intrinsically unstable hydrogen/air flames [8] showed that thermodiffusive instabilities intensify near-wall heat losses and largely alter the flame structure. In more complex high-temperature devices, such as steam-reforming reactors, pronounced non-uniformities in thermal stress have been reported in [9], resulting in structural deflection and crack initiation. The coupling between flame and solid material is strongly bidirectional. For instance, experiments and simulations of pressurized combustors [10] showed that wall vibration can amplify combustion instabilities, thereby increasing the risk of fatigue failure. Transient thermochemical processes such as startup, shutdown or load shifting of thermal systems can impose rapid thermal loading variation and the associated thermo-mechanical stresses, accelerating material degradation over operational cycles [11,12]. The present flame–solid interaction problem is also closely related to a broader class of combustion phenomena involving thermal feedback between a reacting flow and a solid material, such as solid-fuel burning and flame spread along surfaces. In these systems, heat transfer from the flame to the solid governs key processes including ignition and extinction, while the thermal response of the material in turn influences the flame structure and propagation behavior. Recent reviews such as [13] have highlighted the central role of such coupled

* Corresponding author.
E-mail address: chunkan.yu@kit.edu (C. Yu).

https://doi.org/10.1016/j.tsep.2026.104770
Received 28 January 2026; Received in revised form 10 May 2026; Accepted 26 May 2026
Available online 1 June 2026

thermal feedback mechanisms in determining system stability and burning limits.

However, accurate prediction of flame–solid interaction requires a physically consistent representation of the thermo-mechanical behavior of the solid material. Fundamental properties such as heat capacity, elastic modulus, and the coefficient of thermal expansion are not independent quantities; rather, they are thermodynamically linked and must obey compatibility relations derived from the Helmholtz energy [14–16]. This framework guarantees that the resulting constitutive relations remain thermodynamically consistent across the entire deformation and temperature range. Such a rigorous formulation is particularly critical here because the temperature fields generated during transient combustion process are highly non-uniform. Relying on independent tabulated material data may violate thermodynamic constraints, potentially yielding unphysical stresses or inconsistent thermal expansion behavior.

Furthermore, the energy balance and the balance of linear momentum are coupled with each other, such that volume changes can also induce an elasto-caloric effect, which is known as Gough-Joule effect. Previous investigations, such as [17], showed this effect in solids subjected to prescribed pressure, temperature and heat-flux boundary conditions, and concluded that its influence on the predicted thermal and displacement fields was negligible for those configurations. In contrast, the key difference in the present work is that the flame is dynamically coupled with the material, rather than being imposed through fixed boundary conditions. During the transient combustion process, the flame structure itself can evolve in response to changes in wall temperature, heat losses and local burning conditions. As a result, the surface heat flux and temperature no longer remain prescribed but instead stem from the interaction between the flame and the wall. Such a configuration introduces a significantly more complex thermo–mechanical coupling, in which deformation of the solid may influence the local temperature field through the Gough–Joule effect, while simultaneously altering the flame behavior. Therefore, it is necessary to re-evaluate whether the Gough–Joule effect remains negligible in this fully coupled flame–solid system, particularly during the transient stages where thermal gradients, material deformation and flame dynamics interact at the same time.

In addition, in most studies, the balance equation of linear momentum for solid materials is commonly treated under the quasi-static assumption, which assumes that inertial effects are negligible [18–20]. While this simplification is often valid for slowly varying thermal environments, its applicability under transient combustion conditions remains uncertain. During combustion, flame temperatures can reach extremely high values and fluctuate rapidly, inducing correspondingly transient thermo-mechanical stresses in the solid. Under such conditions, the validity of the quasi-static approximation in fully coupled flame–solid systems requires careful evaluation as well.

The objective of the present work is therefore to develop a thermodynamically consistent modeling framework for fully coupled flame–solid interaction and to investigate the transient heating process and the resulting thermo-elastic response of a solid wall. Particular emphasis is placed on (i) the role of the strain rate in the flame in controlling heat transfer and stress development, (ii) the validity of commonly used modeling assumptions such as the quasi-static approximation, and (iii) the relevance of elastic-caloric coupling mechanisms such as the Gough–Joule effect. To investigate these questions, a simple yet realistic combustion configuration, namely a laminar strained premixed flame stabilized at a plane wall, is considered. Heat loss from the flame to the wall is explicitly taken into account, and the resulting temperature variations give rise to combustion-induced thermo-mechanical deformation and stress development within the solid. The study is divided into two main parts. First, the steady-state configuration is examined, with particular emphasis on the effect of thermal radiation on the temperature distribution inside the plane wall. Second, and more importantly, the transient heating process is investigated. In this scenario, a cold plane wall is suddenly introduced into the flame system and subsequently heated, and the entire heating process is analyzed under varying imposed flame strain rates, representing different flow velocities. The validity of the quasi-static assumption in the balance equation of linear momentum and the role of the Gough–Joule effect are examined in detail.

Throughout the whole work, Inconel 718 is selected as a representative solid material due to its excellent mechanical strength, thermal stability, and widespread use in high-temperature combustion and energy-conversion applications [21–23]. The temperature-dependent thermo-physical properties of Inconel 718, including the bulk modulus, shear modulus, thermal conductivity, heat capacity and coefficient of thermal expansion, are represented by fitted functions of temperature. These fits are constructed in a thermodynamically consistent manner based on the Helmholtz energy formulation, ensuring physically meaningful coupling between the thermal and mechanical responses of the solid during the flame–wall interaction.

Furthermore, ammonia/hydrogen blends have attracted increasing attention since they are considered as promising carbon-free energy carriers for next-generation combustion systems [24–26]. Compared to conventional hydrocarbon fuels, ammonia/hydrogen mixtures show fundamentally different combustion characteristics, including different heat release behavior [27,28] and strong preferential diffusion effects arising from the large disparity in molecular diffusivities between ammonia and hydrogen [29–31]. These features can significantly alter flame structure, stability and extinction behavior. As a result, understanding flame–solid interaction in such fuel systems is of particular importance for the development of future zero-carbon combustion technologies.

Notation: Throughout the whole work, a symbolic tensor notation is used:

- Scalar quantities are denoted by lower and upper case Latin and Greek letters, e.g., T, K, G, ρ, ψ;
- Vectors and tuples are denoted by bold lower case Latin letters, e.g., $\boldsymbol{q}$, $\boldsymbol{y}$, $\boldsymbol{f}$;
- Second-order tensors are denoted by bold Greek letters and bold upper case Latin letters, e.g., $\boldsymbol{\varepsilon}$, $\boldsymbol{\sigma}$, $\boldsymbol{\beta}$, $\boldsymbol{A}$, $\boldsymbol{B}$;
- Fourth-order tensors are denoted by upper case blackboard bold Latin Letters, e.g. $\mathbb{A}$, $\mathbb{B}$ and $\mathbb{C}$.

Dot products such as $\boldsymbol{\sigma} \cdot \boldsymbol{\varepsilon}$ are scalar products, regardless of tensor order. The linear mapping of a second order tensor by a fourth order tensor is written as $\mathbb{A}[\boldsymbol{\varepsilon}]$, and the dyadic product between two tensors as $\boldsymbol{A} \otimes \boldsymbol{B}$.

2. Linear thermoelasticity: Thermodynamic treatment

2.1. Fundamentals of thermoelasticity

In the following, a thermodynamically consistent framework to model the thermoelastic wall is introduced. Here, the independent field variables under consideration are the displacement $\boldsymbol{u}(\boldsymbol{x}, t)$ and the temperature $T(\boldsymbol{x}, t)$. Their evolution is governed by the balance equations of linear and angular momentum and the balance equation of internal energy. For small deformations, i.e., $\|\boldsymbol{H}\| \ll 1$, where $\boldsymbol{H} = \partial \boldsymbol{u} / \partial \boldsymbol{x}$ is the displacement gradient, the balance equations can be written as

$$\rho_0 \ddot{\boldsymbol{u}} = \rho_0 \boldsymbol{b} + \operatorname{div}(\boldsymbol{\sigma}), \tag{1}$$

$$\boldsymbol{\sigma} = \boldsymbol{\sigma}^{\mathsf{T}} \tag{2}$$

$$\rho_0 \dot{e} = \rho_0 w - \operatorname{div}(\boldsymbol{q}) + \boldsymbol{\sigma} \cdot \dot{\boldsymbol{\varepsilon}}, \tag{3}$$

where the mass density can be approximated by a constant density $\rho = \rho_0 (1 - \operatorname{tr}(\boldsymbol{\varepsilon})) \approx \rho_0$ (see e.g., [32]). Here, $\boldsymbol{b}$ and w are the mass force density and the specific heat source, respectively, and their values are assumed to be known. The Cauchy stress is denoted by $\boldsymbol{\sigma}$, the heat

flux vector by $\boldsymbol{q}$ and the infinitesimal strain tensor by $\boldsymbol{\varepsilon} = \mathrm{sym}(\boldsymbol{H})$. The material derivative is denoted by a superimposed dot and $\mathrm{tr}(\boldsymbol{\varepsilon})$ denotes the trace of the strain tensor. In order to determine the field variables $\boldsymbol{u}$ and T through the balances of linear momentum and internal energy, appropriate constitutive equations for $\boldsymbol{\sigma}$, $\boldsymbol{q}$ and e are needed. In this work, we focus on thermoelastic simple materials, as introduced in depth, for example, in [33]. Within this framework, all constitutive variables are assumed to be functions of the infinitesimal strain tensor $\boldsymbol{\varepsilon}$, the temperature T and the temperature gradient $\boldsymbol{g}$, i.e.,

$$\begin{aligned} &\psi = \hat{\psi}(\boldsymbol{\varepsilon}, T, \boldsymbol{g}), \quad \eta = \hat{\eta}(\boldsymbol{\varepsilon}, T, \boldsymbol{g}), \\ &\boldsymbol{q} = \hat{\boldsymbol{q}}(\boldsymbol{\varepsilon}, T, \boldsymbol{g}), \quad \boldsymbol{\sigma} = \hat{\boldsymbol{\sigma}}(\boldsymbol{\varepsilon}, T, \boldsymbol{g}), \end{aligned} \tag{4}$$

with the specific entropy η and the specific Helmholtz energy $\psi = e - T\eta$. The material behavior is generally constrained by the second law of thermodynamics, which states that the specific entropy production p_η, occurring in the balance of entropy

$$\rho_0 \dot{\eta} = \rho_0 \frac{w}{T} - \mathrm{div}\left(\frac{\boldsymbol{q}}{T}\right) + \rho_0 p_\eta, \tag{5}$$

must be non-negative, i.e., $p_\eta \geq 0$ (see e.g., [32]). This can be exploited within the Coleman–Noll procedure [34], which results in necessary conditions for the constitutive functions. Here, we start by combining Eqs. (3) and (5) to obtain the Clausius–Duhem inequality

$$\frac{1}{\rho_0}\boldsymbol{\sigma} \cdot \dot{\boldsymbol{\varepsilon}} - \dot{\psi} - \eta \dot{T} - \frac{1}{\rho_0 T}\boldsymbol{q} \cdot \boldsymbol{g} \geq 0. \tag{6}$$

Substituting the functional dependencies (see Eq. (4)) leads to

$$\begin{aligned} &\left(\frac{\boldsymbol{\sigma}}{\rho_0} - \frac{\partial \psi}{\partial \boldsymbol{\varepsilon}}\right) \cdot \dot{\boldsymbol{\varepsilon}} - \left(\eta + \frac{\partial \psi}{\partial T}\right) \dot{T} - \frac{\partial \psi}{\partial \boldsymbol{g}} \cdot \dot{\boldsymbol{g}} \\ &- \frac{1}{\rho_0 T}\boldsymbol{q} \cdot \boldsymbol{g} \geq 0. \end{aligned} \tag{7}$$

This inequality must hold for arbitrary thermodynamic processes [34] yielding the potential relations for the stress tensor and the entropy as

$$\rho_0 \frac{\partial \psi}{\partial \boldsymbol{\varepsilon}} = \boldsymbol{\sigma}, \quad \frac{\partial \psi}{\partial T} = -\eta, \tag{8}$$

as well as the remaining dissipation inequality

$$-\boldsymbol{q} \cdot \boldsymbol{g} \geq 0, \tag{9}$$

providing an additional restriction to the modeling of the heat flux vector $\boldsymbol{q}$. Additionally, it follows that $\partial \psi / \partial \boldsymbol{g} = \boldsymbol{0}$, i.e., ψ and consequently η and $\boldsymbol{\sigma}$ are independent of $\boldsymbol{g}$. Introducing the relations of Eq. (8) as well as the definition of ψ into the balance equation for the internal energy (Eq. (3)) gives the heat conduction equation for the temperature T as

$$\rho_0 c_\varepsilon \dot{T} = \rho_0 w - \mathrm{div}(\boldsymbol{q}) - T\boldsymbol{\beta} \cdot \dot{\boldsymbol{\varepsilon}}, \tag{10}$$

with the heat capacity for constant strain $c_\varepsilon = -T\partial^2 \psi / \partial T^2$ and the coefficient of thermal stress $\boldsymbol{\beta} = -\rho_0 \partial^2 \psi / \partial \boldsymbol{\varepsilon} \partial T = -\partial \boldsymbol{\sigma} / \partial T$ (see Table 1). Furthermore, we assume the standard Hooke's Law

$$\boldsymbol{\sigma}(\boldsymbol{\varepsilon}, T) = \mathbb{C}(T)[\boldsymbol{\varepsilon} - \boldsymbol{\varepsilon}_{\mathrm{th}}(T)], \tag{11}$$

in which $\mathbb{C}$ denotes the elasticity tensor of fourth order, to be valid. Here, the thermal strain $\boldsymbol{\varepsilon}_{\mathrm{th}}$ can be related to the thermal expansion coefficient $\boldsymbol{\alpha}$ as

$$\frac{\mathrm{d}\boldsymbol{\varepsilon}_{\mathrm{th}}}{\mathrm{d}T} = \boldsymbol{\alpha}(T). \tag{12}$$

Therefore, Eq. (11) can be rewritten as

$$\boldsymbol{\sigma}(\boldsymbol{\varepsilon}, T) = \mathbb{C}(T)[\boldsymbol{\varepsilon}] - \boldsymbol{A}(T), \tag{13}$$

with the thermal stress

$$\boldsymbol{A}(T) = \mathbb{C}(T)\left[\int_{T_0}^{T} \boldsymbol{\alpha}\left(\tilde{T}\right) \mathrm{d}\tilde{T}\right]. \tag{14}$$

Table 1
Thermodynamic coefficients.

Quantity	Relation
thermal stress coefficient	$\boldsymbol{\beta}(\boldsymbol{\varepsilon}, T) = -\rho_0 \frac{\partial^2 \psi}{\partial \boldsymbol{\varepsilon} \partial T}$
heat capacity	$c_\varepsilon(\boldsymbol{\varepsilon}, T) = -T \frac{\partial^2 \psi}{\partial T^2}$
elasticity tensor	$\mathbb{C}(T) = \rho_0 \frac{\partial^2 \psi}{\partial \boldsymbol{\varepsilon}^2}$

Using the relation of Eq. (8) the correlation between the elasticity tensor and the Helmholtz energy can be derived as

$$\mathbb{C}(T) = \frac{\partial \boldsymbol{\sigma}}{\partial \boldsymbol{\varepsilon}} = \rho_0 \frac{\partial^2 \psi}{\partial \boldsymbol{\varepsilon}^2}. \tag{15}$$

Lastly, by using the definition of the thermal stress coefficient, also a relation between $\boldsymbol{\alpha}$ and $\boldsymbol{\beta}$ can be established as

$$\begin{aligned} &\boldsymbol{\beta}(\boldsymbol{\varepsilon}, T) = \mathbb{C}(T)[\boldsymbol{\alpha}(T)] - \mathbb{C}'(T)[\boldsymbol{\varepsilon}] \\ &+ \mathbb{C}'(T)\left[\int_{T_0}^{T} \boldsymbol{\alpha}\left(\tilde{T}\right) \mathrm{d}\tilde{T}\right], \end{aligned} \tag{16}$$

with the abbreviation $(\cdot)' = \mathrm{d}(\cdot)/\mathrm{d}T$ being used from this point on.

2.2. Isotropic thermoelastic materials

For further simplification, this study focuses on isotropic material behavior. In this case, the free energy $\psi(T, \boldsymbol{\varepsilon})$, as well as its associated properties (see Table 1), are isotropic functions of $\boldsymbol{\varepsilon}$ and T. For linear elastic materials, the elasticity tensor $\mathbb{C}$ depends only on T and is independent of $\boldsymbol{\varepsilon}$. It can therefore then be represented as

$$\mathbb{C}(T) = 3K(T)\mathbb{P}_1 + 2G(T)\mathbb{P}_2, \tag{17}$$

with the bulk modulus K, the shear modulus G, and the spherical and deviatoric projectors, $\mathbb{P}_1$ and $\mathbb{P}_2$, respectively, defined as $\mathbb{P}_1 = 1/3\, \boldsymbol{I} \otimes \boldsymbol{I}$ and $\mathbb{P}_2 = \mathbb{I}^{\mathrm{sym}} - \mathbb{P}_1$, in which $\boldsymbol{I}$ is the identity tensor of second order and $\mathbb{I}^{\mathrm{sym}}$ denotes the identity tensor of fourth order on the subspace of symmetric second order tensors. Based on this, $\mathbb{C}[\boldsymbol{\varepsilon}] = 3K\boldsymbol{\varepsilon}^{\mathrm{sph}} + 2G\boldsymbol{\varepsilon}^{\mathrm{dev}}$ holds true, where we have introduced the spherical and deviatoric part of the strain tensor as $\boldsymbol{\varepsilon}^{\mathrm{sph}} = 1/3\,\mathrm{tr}(\boldsymbol{\varepsilon})\boldsymbol{I}$ and $\boldsymbol{\varepsilon}^{\mathrm{dev}} = \boldsymbol{\varepsilon} - \boldsymbol{\varepsilon}^{\mathrm{sph}}$, respectively. It should be further pointed out that for isotropic materials, the bulk and the shear modulus can be expressed in terms of the Young's modulus E and the Poisson's ratio ν as $K = E/(3(1-2\nu))$ and $G = E/(2(1+\nu))$. Additionally, for linear thermoelastic materials, the thermal expansion tensor $\boldsymbol{\alpha}$ is also solely a function of temperature. Due to the isotropy, it can then be simplified as

$$\boldsymbol{\alpha}(T) = \alpha(T)\boldsymbol{I} \tag{18}$$

where α is the scalar-valued coefficient of thermal expansion. Due to the definition of the thermal stress (see Eq. (14)), the same holds true in this case and it can be simplified as $\boldsymbol{A}(T) = A(T)\boldsymbol{I}$. By inserting Eqs. (17) and (18) into Eq. (16), the relation between $\boldsymbol{\beta}(T, \boldsymbol{\varepsilon})$ and $\alpha(T)$ can be derived as

$$\begin{aligned} &\boldsymbol{\beta}(\boldsymbol{\varepsilon}, T) = 3K(T)\alpha(T)\boldsymbol{I} - 2G'(T)\boldsymbol{\varepsilon}^{\mathrm{dev}} \\ &+ 3K'(T)\left(\int_{T_0}^{T} \alpha\left(\tilde{T}\right) \mathrm{d}\tilde{T}\boldsymbol{I} - \boldsymbol{\varepsilon}^{\mathrm{sph}}\right). \end{aligned} \tag{19}$$

Lastly, since the heat capacity c_ε is a scalar-valued function of $\boldsymbol{\varepsilon}$ and T one can show (see e.g., [35]) that in the isotropic case

$$c_\varepsilon(\boldsymbol{\varepsilon}, T) = c_\varepsilon(I(\boldsymbol{\varepsilon}), II(\boldsymbol{\varepsilon}), III(\boldsymbol{\varepsilon}), T) \tag{20}$$

holds, where $\{I, II, III\}$ is a set of linearly independent invariants of $\boldsymbol{\varepsilon}$, e.g., the principal invariants of $\boldsymbol{\varepsilon}$.

2.3. Thermodynamically consistent polynomial functions

Since the material coefficients c_ε, $\mathbb{C}$, $\boldsymbol{\beta}$ and implicitly also $\boldsymbol{\alpha}$ are all derivatives of the Helmholtz energy ψ, they cannot be modeled independently. To formulate the resulting restrictions, we start by integrating the potential relation for the stress tensor (Eq. (8)) in combination with Eq. (13) receiving

$$\rho_0\psi(\boldsymbol{\varepsilon},T) = \rho_0\psi_\varepsilon(\boldsymbol{\varepsilon},T) + \rho_0\psi_T(T) + \rho_0\psi_0, \tag{21}$$

with

$$\rho_0\psi_\varepsilon = \frac{1}{2}K(T)\,\mathrm{tr}(\boldsymbol{\varepsilon})^2 + G(T)\left(\|\boldsymbol{\varepsilon}\|^2 - \frac{1}{3}\mathrm{tr}(\boldsymbol{\varepsilon})^2\right) - A(T)\,\mathrm{tr}(\boldsymbol{\varepsilon}) + \frac{1}{2}A(T)^2\,\frac{1}{K(T)}. \tag{22}$$

This leads to the expression for the heat capacity as

$$\begin{aligned}\frac{1}{T}\rho_0 c_\varepsilon =& -\frac{1}{2}K''(T)\,\mathrm{tr}(\boldsymbol{\varepsilon})^2 \\ & -G''(T)\left(\|\boldsymbol{\varepsilon}\|^2 - \frac{1}{3}\mathrm{tr}(\boldsymbol{\varepsilon})^2\right) \\ & +A''(T)\,\mathrm{tr}(\boldsymbol{\varepsilon}) - \rho_0\psi_T''(T) \\ & -A''(T)\,A(T)\,\frac{1}{K(T)} \\ & -A'(T)\,A'(T)\,\frac{1}{K(T)} \\ & +2A'(T)\,A(T)\,\frac{1}{K(T)^2}K'(T) \\ & -A(T)\,A(T)\,\frac{1}{K(T)^3}K'(T)\,K'(T) \\ & +\frac{1}{2}A(T)\,A(T)\,\frac{1}{K(T)^2}K''(T),\end{aligned} \tag{23}$$

which can be split into a purely temperature-dependent and a mixed strain- and temperature-dependent part, i.e.,

$$\rho_0 c_\varepsilon(\boldsymbol{\varepsilon},T) = \rho_0 c_{\varepsilon T}(T) + \rho_0 c_{\varepsilon\varepsilon}(\boldsymbol{\varepsilon},T). \tag{24}$$

Based on the experimental data of the here investigated material Inconel 718, as will be discussed in detail in section 6, a linear approximation of K, G, α and $c_{\varepsilon T}$ is sufficient within the relevant temperature range between 300K to 700K. In the isotropic case this leads to the following equations

$$\mathbb{C} = \left(3K_1\Delta T + 3K_0\right)\mathbb{P}_1 + \left(2G_1\Delta T + 2G_0\right)\mathbb{P}_2 \tag{25}$$

$$\boldsymbol{\alpha} = \alpha\boldsymbol{I} = \left(\alpha_1\Delta T + \alpha_0\right)\boldsymbol{I} \tag{26}$$

$$c_{\varepsilon T} = c_{\varepsilon T1}\Delta T + c_{\varepsilon T0} \tag{27}$$

with the set of constant parameters $\{K_1, K_0, G_1, G_0, \alpha_1, \alpha_0, c_{\varepsilon T1}, c_{\varepsilon T0}\}$ to be fitted to experimental data. From Eq. (14), it follows that in this case the thermal stress $\boldsymbol{A}$ is a cubic polynomial in T of the form

$$\begin{aligned}\boldsymbol{A}(T) &= \left(A_3\Delta T^3 + A_2\Delta T^2 + A_1\Delta T\right)\boldsymbol{I} \\ &= \Big(\frac{3}{2}K_1\alpha_1\Delta T^3 + \left(3K_1\alpha_0 + \frac{3}{2}K_0\alpha_1\right)\Delta T^2 + 3K_0\alpha_0\Delta T\Big)\boldsymbol{I}.\end{aligned} \tag{28}$$

With this, the remaining part of the heat capacity, $c_{\varepsilon\varepsilon}$, is fully determined as

$$\rho_0 c_{\varepsilon\varepsilon}(\boldsymbol{\varepsilon},T) = T\left(9K_1\alpha_1\Delta T + 3K_0\alpha_1 + 6K_1\alpha_0\right)\mathrm{tr}(\boldsymbol{\varepsilon}), \tag{29}$$

and cannot be chosen independently.

3. Mathematical model for simulation of strained premixed flame in stagnation flow

The numerical simulation of the strained premixed flame is performed using the in-house INSFLA code [36], which has been extensively validated against fundamental combustion characteristics, including laminar flame speeds [37,38] and flame extinction limits [39], as well as transient combustion processes such as head-on quenching [40]. In the present section, only the governing equations and key concepts relevant to the current study, such as the definition of flame strain rate, are briefly reviewed to facilitate the discussion of the flame–solid interaction phenomena presented later. Further details regarding the numerical implementation and validation of the solver can be found in the corresponding literature [36,41].

3.1. Governing equations in general form

The conservation equations for one-dimensional strained flames in a general nonsteady case used in the present numerical simulation follow those proposed in [41], which were derived including two parameters (tangential pressure gradient J and tangential velocity gradient G). Based on the derivation in [41], although the flow field is two-dimensional (2D), all thermo-kinetic quantities (e.g., temperature T_g, pressure p_g, gas mixture density ρ_g, species mass fractions $\boldsymbol{y}$) of the flame can be simplified to one-dimensional (1D) along the symmetric line and are functions of the z-coordinate. Thus, the resulting set of nonsteady governing equations for strained flames read

$$\dot{\rho}_g = -2\rho_g G - \frac{\partial(\rho_g v_z)}{\partial z}, \tag{30}$$

$$\rho_g\dot{G} = -J - \rho_g G^2 + \frac{\partial}{\partial z}\left(\eta_g\frac{\partial G}{\partial z}\right) - \rho_g v_z\frac{\partial G}{\partial z}, \tag{31}$$

$$\rho_g c_{p,g}\dot{T}_g = -j_g^q - \dot{\boldsymbol{r}}\cdot\bar{\boldsymbol{h}} - \rho_g c_{p,g} v_z\frac{\partial T_g}{\partial z} - \dot{q}_{\mathrm{rad}}, \tag{32}$$

$$\rho_g\dot{\boldsymbol{y}} = -\frac{\partial \boldsymbol{j}_g^s}{\partial z} + \dot{\boldsymbol{r}}\cdot\boldsymbol{m}_w - \rho_g v_z\frac{\partial \boldsymbol{y}}{\partial z}, \tag{33}$$

$$0 = \rho_g - \frac{p_g\bar{M}}{RT_g}. \tag{34}$$

In these equations, v_x and v_z are the flow velocities in the radial and axial directions. η_g is the dynamic viscosity, and $c_{p,g}$ is the isobaric heat capacity. $\boldsymbol{r}$, $\bar{\boldsymbol{h}}$, and $\boldsymbol{m}_w$ denote the chemical source term, specific enthalpy, and molar mass involving all species. j_g^q is the energy transport flux, which can be calculated as:

$$j_g^q = -k\frac{\partial T}{\partial z} + \boldsymbol{c}_p\cdot\boldsymbol{j}_g^s, \tag{35}$$

in which $\boldsymbol{c}_p$ is the tupel including the isobaric heat capacity of all species, and $\boldsymbol{j}_g^s$ is the molecular diffusion flux including the differential diffusion and thermal diffusion (Soret effect) [42].

For the one-dimensional counterflow configuration considered here, the imposed strain rate in the flame a (in the following: flame strain rate) is characterized by the velocity gradient acting on the flame front and serves as a measure of the aerodynamic stretching imposed on the flame. According to [41], the tangential pressure gradient J is correlated with the flame strain rate as: $a = \sqrt{-J/\rho_{\mathrm{ub}}}$, where ρ_{ub} is the density of the unburned gas. More details and derivations can be found in [41].

3.2. Optically thin approximation radiation model (OTM)

In Eq. (32), the volumetric heat loss due to thermal radiation, $\dot{q}_{\mathrm{rad}}$, is also taken into account, as thermal radiation may influence the flame structure and properties and serve as an additional external source that can potentially impact the temperature of surrounding materials,

especially in high-temperature environments. In the present work, the simple optically thin approximation model (OTM) is used to predict the volumetric radiative heat loss in W/(m^3) and given as:

$$\dot{q}_{\mathrm{rad}} = 4\, k_p\, \sigma\, \left(T_g^4 - T_{\mathrm{b}}^4\right), \tag{36}$$

in which $\sigma = 5.669 \cdot 10^{-8}\mathrm{W/(m^2{\cdot}K^4)}$ is the Stefan–Boltzmann constant, and T_{b} the background temperature. k_p are the total Planck mean absorption coefficient and calculated as $k_p = \boldsymbol{p}_p \cdot \boldsymbol{a}_p$, where $\boldsymbol{p}_p$ are the partial pressures and $\boldsymbol{a}_p$ is the Planck mean absorption coefficients of all radiating species. These coefficients can be estimated using HITRAN database [43].

4. Boundary conditions at interface

To establish a consistent coupling between the gas-phase flame and the solid-phase material, it is essential to clearly define the boundary conditions applied at their interface. We denote the interface position by I. The notation I^- refers to the solid-side limit approaching the interface, while I^+ represents the gas-side limit of the flame adjacent to the wall.

With this notation in place, we can systematically formulate the governing interfacial constraints. We first introduce the temperature boundary condition, which ensures thermodynamic continuity between gas and solid. This is followed by the species boundary condition, describing how chemical species behave at a non-permeable and inert surface. Finally, we present the mechanical boundary condition at the interface, which enforces the mechanical equilibrium at the interface between the gas-phase flame regime and the solid-phase material regime.

4.1. Temperature

For the thermal field, it is assumed that the interface satisfies thermal equilibrium conditions, which can be formulated through the following two requirements:

(i) Continuity of temperature: The temperature field must remain continuous across the interface: $T(z = \mathrm{I}^-) = T(z = \mathrm{I}^+)$.

(ii) Balance of energy transport flux: At the interface, the energy transport flux from the flame side must equal the energy transport flux into the wall surface, taking into account conductive and radiative heat transfer contributions. This suggests the relation: $j_q(z = \mathrm{I}^-) = j_q(z = \mathrm{I}^+) + \alpha j_{\mathrm{rad}}$, in which j_{rad} is the radiant heat flux emitted by the flame and received by the wall surface, and α is the absorptance of the wall surface varying from 0.0 to 1.0. For the radiant heat flux, it can be assumed that all the radiative heat loss will reach the wall surface and can be determined as $j_{\mathrm{rad}} = \int_{\mathrm{I}^+}^{\infty} \dot{q}_{\mathrm{rad}} \mathrm{d}z$.

The assumption that the entire radiative heat loss reaches the wall surface represents an extreme upper-limit estimate for the radiative contribution. This simplification is justified for the present analysis for the following reason. As shown later, the conductive heat flux from the flame to the wall dominates the overall heat transfer, while the radiative component is significantly smaller at the interface. By considering the extreme case in which all radiative heat emitted toward the wall is fully absorbed at the interface, the influence of radiation is intentionally overestimated. Consequently, if the radiative contribution is shown to be negligible even under this upper-bound assumption, its actual effect in realistic situations where part of the emitted radiation would not reach or be absorbed by the wall will be even smaller. Therefore, this assumption does not affect the generality of the conclusions and provides a conservative estimate of the role of radiation in the present configuration.

4.2. Species concentrations

In the present study, we assume a non-permeable wall surface, such that no chemical species can penetrate into the solid material, and an inert surface, meaning that no heterogeneous or surface chemical reactions take place at the wall. Under these assumptions, the species boundary condition on the gas-phase side of the interface reduces to

$$\boldsymbol{j}_g^s(z = \mathrm{I}^+) = 0. \tag{37}$$

These assumptions are introduced to keep the present analysis focused on the coupled thermo-mechanical response of the heated solid. Allowing for species adsorption, desorption, catalytic reactions or finite wall permeability would require additional reaction-transport modeling at the interface and would significantly increase the complexity of the formulation. Since the primary objective of this work is to investigate the flame–solid thermal interaction and the resulting stress development in the solid, such effects are beyond the scope of the current study.

4.3. Mechanical stress

At the interface, the balance of normal forces requires that the normal stress in the solid equals the gas pressure from the flame on the wall surface. Since no tangential loading arises in the present one-dimensional configuration, only the normal component of the stress tensor contributes at the interface and the stress boundary condition reduces to

$$\sigma_{zz}(\mathrm{I}^-) = -p_g(\mathrm{I}^+). \tag{38}$$

5. Gas mixture and chemical kinetic model

In this work, we investigate a stoichiometric premixed ammonia–air mixture with 40% hydrogen addition. The unburnt mixture composition is $0.4\mathrm{H_2} + 0.6\mathrm{NH_3} + 0.65(\mathrm{O_2} + \frac{79}{21}\mathrm{N_2})$, which corresponds to stoichiometric conditions based on the overall reaction of ammonia/hydrogen oxidation in air. The addition of hydrogen is known to enhance the reactivity of ammonia–air flames, reduce ignition delay and increase flame stability against extinction [24].

Regarding radiative properties, the present study accounts for the dominant radiating species identified for ammonia–hydrogen–air combustion. According to Nakamura et al. [44], $\mathrm{H_2O}$, NO, $\mathrm{N_2O}$, and $\mathrm{NH_3}$ constitute the four major contributors to gas-phase radiation within this mixture. Their corresponding Planck mean absorption coefficients are provided in [44], which are derived from spectroscopic HITRAN databases [43]. These values are then applied in the radiation model to evaluate radiative heat loss from the flame to the wall surface.

The chemical kinetic model used for simulating the premixed flame is adopted from [45]. This mechanism has been validated against experimental measurements for ammonia/hydrogen combustion and captures the essential elementary reactions governing fuel oxidation and NOx formation. In the present study, it is used without modification to ensure consistency with well-established chemical kinetics for ammonia–hydrogen flames.

6. Solid material

Inconel 718 is chosen as the wall material due to its excellent thermo-mechanical performance under high-temperature conditions. As a nickel-based superalloy, it maintains high yield strength and structural stability at elevated temperatures [21,22], making it widely used in combustors and gas turbine components [23,46,47]. Moreover, its well-documented temperature-dependent material properties of Inconel 718 further enable reliable and thermodynamically consistent solid modeling in the present work.

Moreover, it should be noted that the temperature range considered in the present study is limited to 300–700 K. This choice is motivated

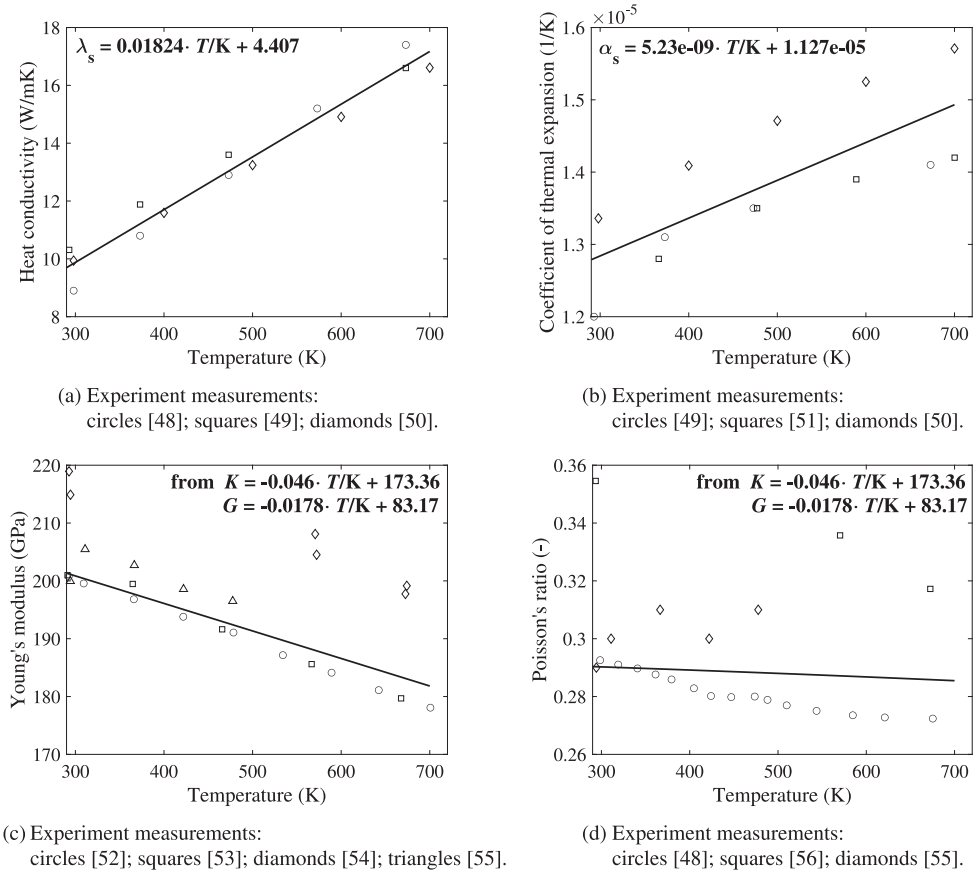

(a) Experiment measurements: circles [48]; squares [49]; diamonds [50].

(b) Experiment measurements: circles [49]; squares [51]; diamonds [50].

(c) Experiment measurements: circles [52]; squares [53]; diamonds [54]; triangles [55].

(d) Experiment measurements: circles [48]; squares [56]; diamonds [55].

Fig. 1. Temperature dependence of (a) heat conductivity λ_s, (b) coefficient of thermal expansion α_s, (c) Young's modulus and (d) Poisson's ratio for Inconel 718. Solid lines: mathematical correlations of experimental data used in the present work; Symbols: experimental measurements from literature with corresponding references, which are stated in the subfigure caption (see [48–54]).

by the fact that, as will be shown later, temperatures exceeding this range lead to the onset of plastic deformation in the material, beyond which the linear thermoelasticity model used in this work is no longer applicable.

Fig. 1 shows the temperature dependence of the thermo-mechanical properties of Inconel 718, including (a) heat conductivity λ_s, (b) coefficient of thermal expansion α_s, (c) Young's modulus E, and (d) Poisson's ratio ν. All thermophysical properties based on experimental data reported in the literature are represented by symbols, and the corresponding sources are indicated through the referenced datasets used for the fitting procedure. And the solid lines denote mathematical correlations of experimental data used in the present simulations. In the thermoelastic formulation adopted in this work, the bulk modulus K and shear modulus G are assumed to be linear functions of temperature (c.f. Eq. (25)). However, most available experimental data are reported in terms of E and ν rather than K and G. Therefore, the linear temperature dependencies of $K(T)$ and $G(T)$ are substituted into the constitutive relations linking (K, G) with (E, ν) (c.f. Eq. (39)), and the resulting expressions for $E(T)$ and $\nu(T)$ are subsequently fitted to the experimental data. This procedure ensures thermodynamic consistency of the material model while preserving agreement with measured temperature-dependent elastic properties.

$$E = \frac{9KG}{3K+G}, \qquad \nu = \frac{3K-2G}{6K+2G}. \tag{39}$$

Fig. 2 (upper) presents the fitted temperature dependence of the heat capacity at constant stress $c_\sigma(T)$ for Inconel 718, together with experimentally measured values reported in the literature. It should be noted, however, that the governing energy equation for the solid (see Eq. (10)) requires the heat capacity at constant strain, c_ε (equivalently, at constant volume), rather than c_σ. The two quantities are related through thermodynamic identities. Specifically, the laws of thermodynamics imply the following relation between the specific heat capacities at constant stress and constant strain [55]:

$$c_\sigma - c_\varepsilon = \frac{\alpha^2 T}{\rho \beta_T}, \tag{40}$$

in which β_T is the isothermal compressibility (the inverse of the bulk modulus). Using this relation, the relative deviation between c_σ and c_ε is evaluated and shown in Fig. 2 (lower). For the temperature range and material considered in the present study, the maximum relative deviation does not exceed 0.55%. This small difference justifies the approximation $c_\varepsilon \approx c_\sigma$ in Eq. (10), allowing the use of the fitted $c_\sigma(T)$ without introducing a noticeable error in the predicted thermal response of the plane wall. Furthermore, it can be easily checked that the term $c_{\varepsilon\varepsilon}$ (c.f. Eq. (29)) is also negligible small for the here fitted material parameters for Inconel 718 and the concurring strains due to the thermal loading.

It should be emphasized at this point that noticeable discrepancies exist among the experimentally reported thermo-mechanical properties of Inconel 718, as shown by the scatter of the measurement data collected from different sources. However, resolving these experimental variations is beyond the scope of the present study. The primary objective here is to ensure a thermodynamically consistent representation of the material behavior, rather than to identify a universally optimal set of material parameters. Within this framework, the adopted fitting strategy provides a systematic and physically consistent way to incorporate temperature-dependent thermo-mechanical properties. Should more accurate or updated experimental data become available

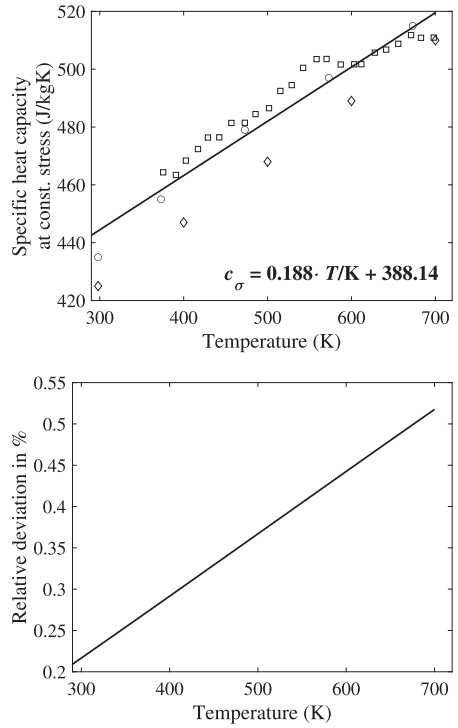

Fig. 2. Upper: Temperature dependence of heat capacity at constant pressure $c_{p,s}$ for Inconel 718. Solid lines: fitted lines; Symbols: experiment measurements with circles [56], squares [57], and diamonds [58]. Below: relative deviation between isobaric and isochoric heat capacity in %.

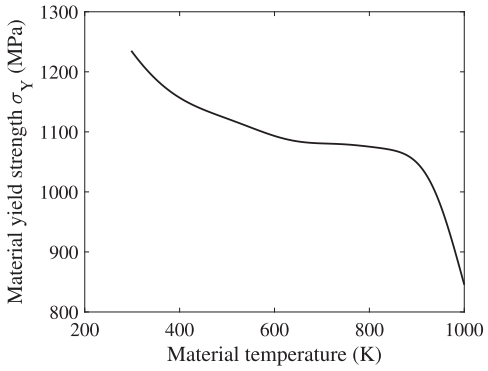

Fig. 3. Temperature dependence of yield strength σ_Y for Inconel 718 from [59].

in the future, the same methodology can be readily applied to re-calibrate these properties without modifying the underlying theoretical formulation.

Since a linear thermoelasticity model is employed in the present study, all computations must be restricted to the thermoelastic regime. It is therefore necessary to identify the material yield strength in order to determine the time at which plastic deformation may potentially occur. Fig. 3 presents the temperature-dependent trend of the yield strength of Inconel 718, as reported in [59]. This information provides a critical reference for assessing the validity of the thermoelastic assumption and for defining the upper temporal limit of the analyzes presented in this work.

7. Results and discussion: Steady-state flame

The steady-state flame–solid configuration considered in this section has been extensively investigated in previous studies, and its

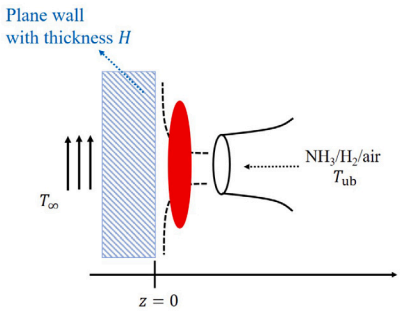

Fig. 4. Illustration of studied steady case for flame–solid interaction based on strained laminar premixed flame stabilized at a plane wall. Fuel/air here is NH_3/H_2/air mixture with NH_3:H_2=60%:40%.

reactive-fluid and thermo-mechanical coupling characteristics are well documented. In particular, the flame–solid thermal interaction associated with this configuration has already been analyzed in detail in our previous works such as [7,60]. Therefore, these aspects are not repeated here. Instead, the present section focuses on a complementary analysis by assessing the influence of thermal radiation on the flame–wall heat transfer under steady-state conditions. This examination serves to clarify the role of thermal radiation in the overall energy balance and allows the subsequent transient heating analysis to be performed without repeatedly revisiting radiation-related effects.

The physical configuration considered here is illustrated in Fig. 4. A one-dimensional strained laminar premixed flame, formed by a stoichiometric NH_3/H_2/air mixture, is stabilized on the right side of a plane wall of thickness H. The wall is placed into the system and interacts thermally with the flame. The coordinate origin is placed at the flame–wall interface, such that the solid domain occupies $-H \le z \le 0^-$ and the gas-phase flame extends to $z \ge 0^+$.

At the cold side of the wall, i.e., at $z = -H$, a convective heat transfer condition is imposed to account for heat exchange with the surrounding environment. The corresponding boundary condition for the heat flux reads $j_q(z = -H) = -h(T(z = -H) - T_\infty)$, where T_∞ represents the ambient temperature.

On the unburnt-gas side of the premixed flame, the thermodynamic state of the incoming mixture is prescribed. Specifically, the temperature, pressure, and species concentrations of the unburnt premixed NH_3/H_2/air mixture are fixed as boundary inputs for the flame calculation.

Throughout all results presented in this section, the operating pressure is kept at $p = 1$ bar, and the plane wall thickness is $H = 1$ cm. The convective heat transfer coefficient at the cold side of the wall is chosen as $h = 1 \cdot 10^3$ W/(m^{2}K) as an example. Note that the conclusion drawn here is also validated, if other convective heat transfer coefficient is chosen.

Fig. 5 (upper) illustrates the typical temperature profiles of the flame and the interior of the plane wall for two different absorptance values, $\alpha = 0.0$ (blue) and $\alpha = 1.0$ (red), under the condition that the strain rate imposed on the premixed flame is $a = 100$ s^{-1}.

Note that here the absorptance coefficient α is not prescribed as a specific temperature-dependent material property. Instead, it is varied between $\alpha = 0.0$ and $\alpha = 1.0$ to cover the full physically admissible range. For $\alpha = 0.0$, no radiative heat flux is absorbed by the plane wall, whereas for $\alpha = 1.0$, all radiative heat flux is fully absorbed by the plane wall. This bounding approach allows us to assess the maximum possible influence of thermal radiation on the flame-wall interaction without relying on uncertain surface property data. Furthermore, thermal emission from the solid surface is neglected. This assumption effectively represents an upper-bound estimate of the net radiative heat input to the wall, ensuring that the influence of radiation is not underestimated.

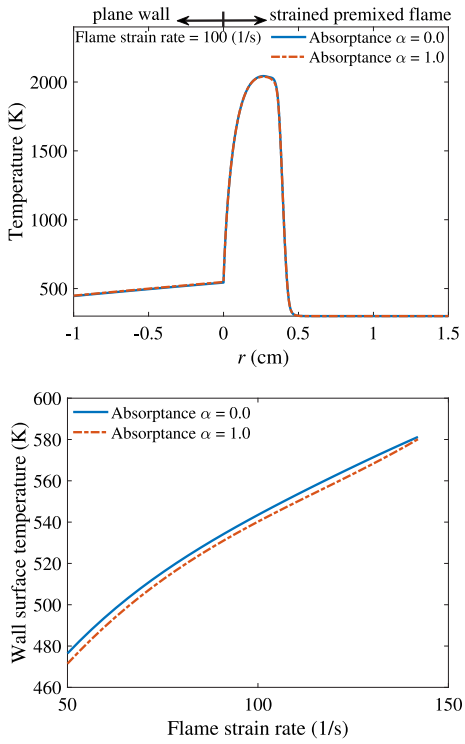

Fig. 5. Upper: Typical temperature profiles of the flame and inside the plane wall with two different absorptance $\alpha = 0.0$ (blue) and $\alpha = 1.0$ (red) for flame strain rate: $a = 100\ \mathrm{s}^{-1}$. Below: Wall surface temperature for varying flame strain rate.

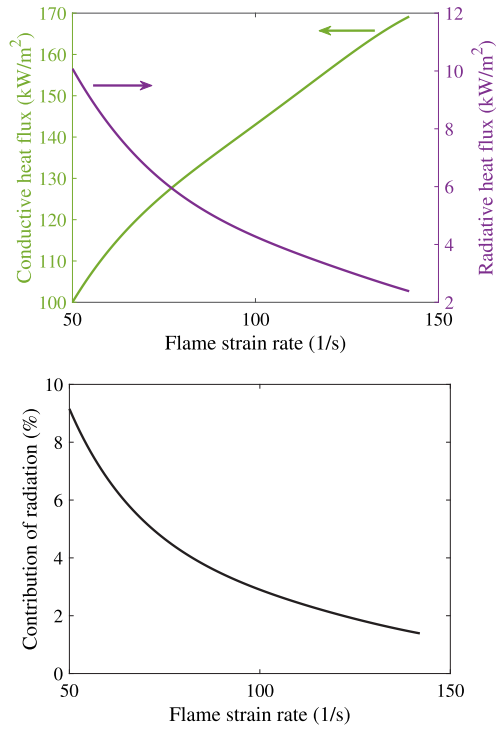

Fig. 6. Comparison of conductive heat flux and radiative heat flux (Upper) and the corresponding contribution of radiative heat flux in % (Lower) for varying flame strain rate.

It is straightforward that the temperature gradient on the plane wall side ($z = 0^-$) is much smaller than that on the flame side ($z = 0^+$), attributing to the significantly higher heat conductivity of the metallic plane wall compared to that of the gas-phase flame. However, it is interesting to note that even when the absorptance value reaches its maximum of 1.0 (indicating full absorption of the thermal radiation emitted from the flame), the temperature at the wall surface and the resulting temperature profile inside the plane wall show only minor changes compared to the case with an absorptance of $\alpha = 0.0$. The minor difference in the temperature profile inside the plane wall with two different absorptance values is further confirmed in Fig. 5 (below), where the dependence of wall surface temperature on the varying flame strain rate up to the extinction strain rate (the rightmost point) is presented. It is clearly observed that the difference in wall surface temperature between the two absorptance values remains within 5 K, which is negligibly small.

In order to understand this phenomenon, we define the quantity *Contribution of Radiation* as the percentage of the radiative heat flux j_{rad} to the total heat flux flowing inside the plane wall at the interface $j_q(z = \mathrm{I}^-)$, which consists of both conductive heat flux at the wall surface ($j_{\mathrm{cond}} = -k\frac{\partial T}{\partial z}\Big|_{z=\mathrm{I}^+}$ from Eq. (35)) and radiative heat flux. Fig. 6 compares the conductive heat flux and radiative heat flux from the flame side for varying flame strain rates in the upper sub-figure, and the corresponding *Contribution of Radiation* in the lower sub-figure.

From the upper sub-figure in Fig. 6, it is observed that the conductive heat flux increases with increasing flame strain rate, whereas the radiative heat flux decreases. These opposite trends can be explained from different perspectives. The increase in conductive heat flux is primarily attributed to the increased temperature gradient at the wall surface, as the flame moves closer to the plane wall with increasing strain rate [7]. On the other hand, the decrease in radiative heat flux is mainly due to the reduction in flame temperature with increasing strain rate [61], leading to a corresponding reduction in radiative heat loss. Interestingly, the proportion of radiative heat loss relative to the total heat flux shows a distinctive behavior in lower sub-figure in Fig. 6: it reaches a maximum of around 10% at low flame strain rates but rapidly reduces to less than 2% as the strain rate increases, which presents the minor role of radiative heat transfer under such conditions. The remarkably low contribution of radiative heat flux, especially at high strain rates, suggests that thermal radiation plays only a minor role in influencing variations in the wall surface temperature. Instead, the primary factor governing wall temperature changes is associated with conductive heat transfer.

8. Results and discussion: Transient process

In this section, the transient process of flame–solid interaction is investigated. Fig. 7 illustrates the configuration which will be studied in the present work. Before the plate is introduced into the system, the setup corresponds to the classic configuration of a laminar premixed strained flame in counterflow, in which two identical streams of premixed fuel–air mixtures are impinging toward each other with equal momentum in the horizontal z-direction. Such counterflow flames are widely used as model systems due to their well-defined strain rate, reasonable one-dimensional structure, and suitability for fundamental investigations of heat transfer, chemical kinetics, response to flow conditions and others [46,62,63]. The unburned mixture consists of stoichiometric ammonia–hydrogen–air, with the fuel composition ratio of 60% NH_3 and 40% H_2 by volume. To provide a clearer understanding of this condition, Fig. 8 presents the temperature profiles of steady laminar premixed flames under different flame strain rates. Here, we emphasize two phenomena that are particularly relevant to the subsequent discussion. Firstly, as the flame strain rate increases, the reaction zone becomes narrower due to the higher flow velocity imposed by the nozzle. Secondly, the convective time scale decreases with increasing strain rate, leaving less time for chemical reactions to occur. As a

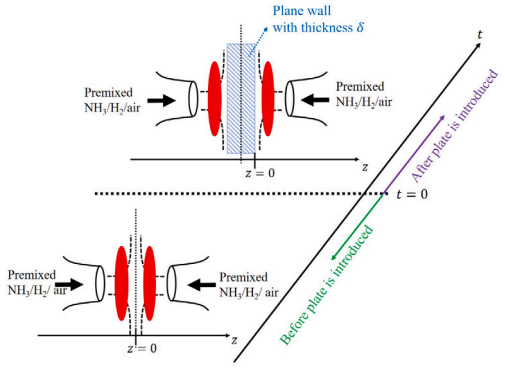

Fig. 7. Illustration of studied transient flame–solid interaction process. Fuel/air here is NH_3/H_2/air mixture with NH_3:H_2=60%:40%.

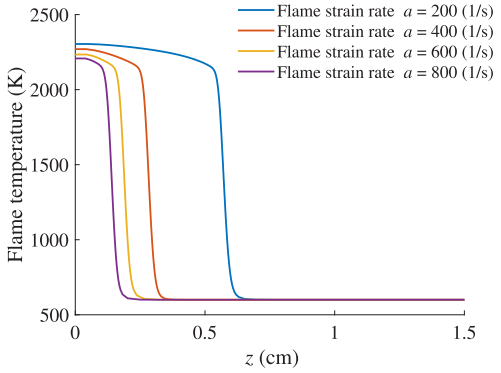

Fig. 8. Temperature profiles of steady laminar premixed flames under different flame strain rates.

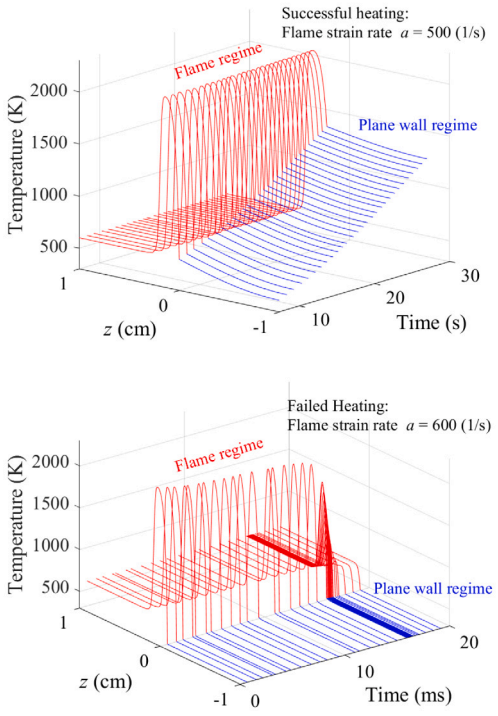

Fig. 9. Temporal evolution of the spatial flame temperature (red profiles) and the temperature distribution inside the plane wall (blue profiles) for two different imposed flame strain rates: flame strain rate a = 500 1/s for successful heating; flame strain rate a = 600 1/s for failed heating.

result, the chemical reaction becomes less complete, leading to a lower maximum temperature at the flame center.

At time $t = 0$, a solid plane wall of thickness $\delta = 2$ cm and initial uniform temperature T_s^0 is suddenly inserted at the center of the burners, coinciding with the location of the stagnation plane. Because the plane wall temperature T_s is significantly lower than the flame temperature, heat is rapidly conducted from the hot flame regime toward the solid plane wall, causing the wall temperature to rise.

8.1. A-priori analysis on transient heating process

Before providing a deeper understanding of the effect of a transient heating process on the thermo-mechanical behavior, we first show *a-priori* how the energy in the combustion system is transported into the plane wall. During this process, the heat absorbed by the plate may potentially lead to flame extinction, since the flame temperature can decrease as energy is continuously conducted into the solid. To illustrate this mechanism, Fig. 9 shows the temporal evolution of the spatial flame temperature (red) and the temperature distribution inside the plane wall (blue) for two different imposed flame strain rates.

For a relatively low strain rate (here $a = 500$ 1/s in upper subfigure), the temperature at the flame–wall interface (i.e., the plane wall surface at $z = 0$) increases continuously. Heat conduction subsequently transports the energy into the plane wall interior, resulting in the temperature increase within the plane wall; however, it is important to note that the temperature field inside the plane wall remains non-uniform, namely the highest temperature is observed at the surface while the minimum temperature occurs at the center.

For a higher strain rate (here $a = 600$ 1/s in lower subfigure), the transient heating process shows significantly different behavior. As mentioned earlier, increasing the flame strain rate leads to less complete rate of chemical reactions, which in turn reduces both the flame temperature and the associated heat release rate. When the plane wall is introduced into the system, the large temperature gradient at the wall surface results in a substantial heat loss from the flame, further lowering the available thermal energy within the combustion zone. As the flame temperature continues to decrease due to this heat loss, the combustion system reaches a thermo-kinetic state where the temperature is insufficient to sustain chemical reactions under the given flow velocity. Consequently, the flame undergoes rapid extinction, which in this case occurs over a timescale of approximately 1 ms.

In the following subsections, we first provide a brief discussion on the influence of flame strain rate on the occurrence of failed heating. We then focus on the successful heating process, during which the wall temperature rises significantly. Such pronounced heating can induce thermal deformation and generate substantial thermomechanical stress, which will be studied in detail.

8.2. Failed heating process

Although flames with a strain rate of 600 1/s or higher can exist under steady-state conditions, the heat loss introduced by placing the plane wall into the system leads to flame extinction. To verify this, Fig. 10 presents the temporal evolution of the maximum flame temperature and the wall-surface temperature (at $z = 0$) for three different flame strain rates. In the present study, flame extinction (or failed heating) is defined based on the temporal evolution of the flame temperature. Specifically, extinction is considered to occur when the flame temperature decreases to the unburnt gas temperature (300 K) over a sufficiently long simulation time (10^5 s throughout the whole work), which is significantly longer than the characteristic timescales of the system. Two clear observations can be made.

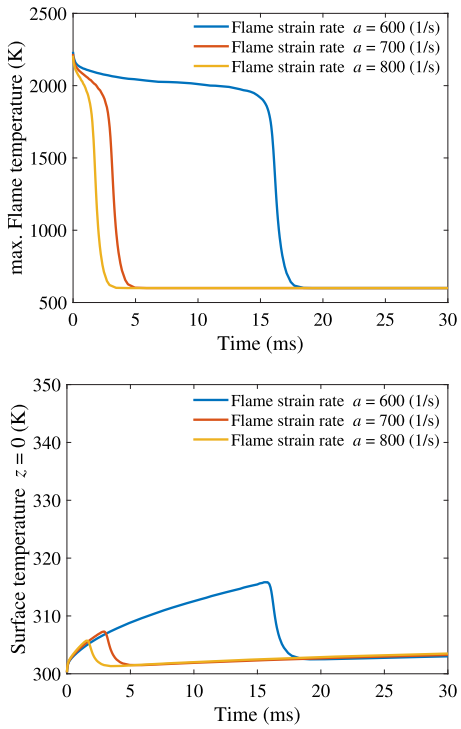

Fig. 10. Temporal evolution of the maximum flame temperature and the wall-surface temperature (at $z = 0$) for three different flame strain rates.

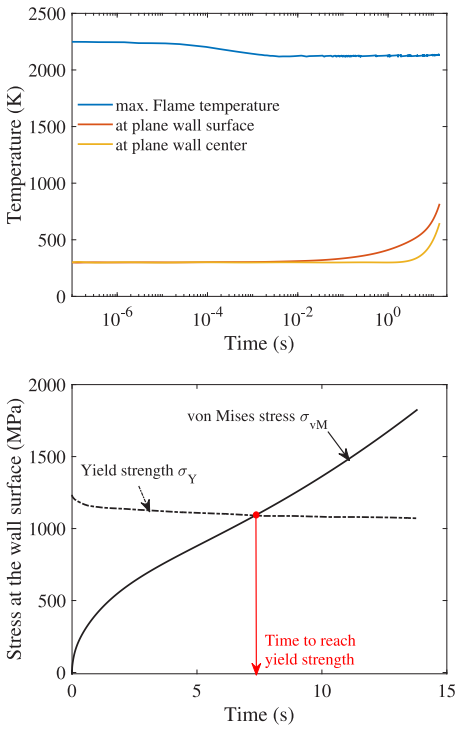

Fig. 11. Upper: transient evolution of the maximum flame temperature, the wall-surface temperature, and the temperature at the plate center; Below: time evolution of the von Mises stress at the wall surface (solid line), together with the corresponding yield strength of the material evaluated at the same wall surface temperature (dashed line). Flame strain rate: $a = 500\ \mathrm{s}^{-1}$.

First, flame extinction occurs more rapidly as the flame strain rate increases. This is because higher strain rates reduce the degree of completeness of chemical reactions, making the chemical reaction within the reaction zone less intensive. Since chemical reactions are strongly temperature-dependent, the additional heat loss to the wall accelerates the reduction in flame temperature, which further suppresses the reaction rate and causes extinction. In other words, with increasing strain rate, the flame becomes increasingly sensitive to heat loss, resulting in a faster extinction process.

Second, during the extinction process, the wall temperature increases only slightly. For example, in the cases shown here, the rise is on the order of around 20 K. This occurs because the flame is extinguished within only several milliseconds, whereas heat conduction within the solid requires a much longer response time. As a result, the material heats up slowly, and when the flame quenches so quickly, the wall does not acquire enough time to experience a substantial temperature increase.

8.3. Successful heating process

In contrast to the failed-heating cases discussed in the previous subsection, where the heat loss to the plate leads to rapid flame extinction, we now focus on the successful heating regime, in which the flame remains stable after the plane wall is introduced and is able to continuously supply thermal energy to the solid. The transition between failed and successful heating can be interpreted as a critical condition governed by the competition between flame heat release and heat loss to the wall, which is primarily controlled by the imposed flame strain rate and the initial wall temperature. A systematic characterization of this transition boundary is however beyond the scope of the present study.

Fig. 11 (upper) shows the transient evolution of the maximum flame temperature, the wall-surface temperature, and the temperature at the plate center for a flame strain rate of 500 1/s. Two features of the successful heating process become evident:

- First, the maximum flame temperature adjusts extremely quickly following the insertion of the plate. Within a very short time, it reaches a value close to its final quasi-steady level. The subsequent evolution shows only a slight change, which results from the heat loss into the plate. This reflects the fast thermal response of the flame compared to the solid.
- In contrast, the temperature inside the plane wall evolves on a much longer timescale. Because of the finite thermal diffusivity of the material, the wall requires a considerably longer time before a noticeable temperature rise occurs. As expected, the wall-surface temperature is consistently higher than the temperature at the plane wall center, since the surface is in direct contact with the flame while heat must conduct inward before affecting the interior.

Having discussed the transient temperature evolution in the successful-heating case, we now examine the development of the resulting thermo-mechanical stress in the plane wall. Because the wall surface experiences the highest temperature during heating, it also undergoes the largest thermal expansion and therefore shows the maximum displacement. Consequently, the von Mises stress at the wall surface is the highest within the plate, and our analysis focuses on this location as representative candidate.

Fig. 11 (below) shows the time evolution of the von Mises stress at the wall surface (solid line), together with the corresponding yield strength of the material evaluated at the same wall surface temperature (dashed line). The red circle indicates the instant at which the von Mises stress becomes equal to the temperature-dependent yield strength. This time is identified as the time to reach yield strength. Beyond this point, the von Mises stress exceeds the yield strength, and the thermoelastic model used in this study is no longer applicable.

It is important to note that the timescale associated with the development of thermo-mechanical stress essentially follows the same

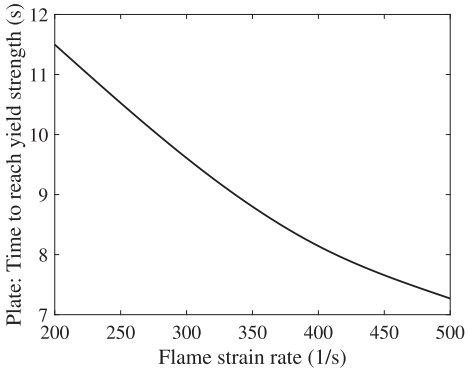

Fig. 12. Time to reach the yield strength σ_Y against different flame strain rate.

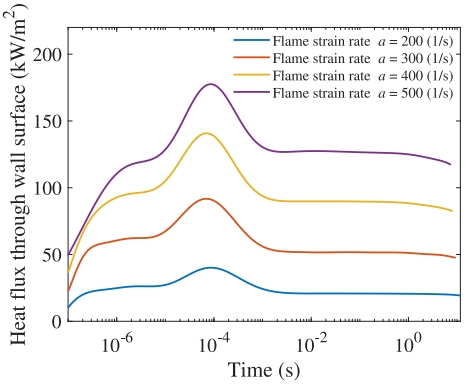

Fig. 13. Temporal evolution of the wall-surface heat flux for different flame strain rates until reaching the yield strength.

timescale as the temperature rise of the plane wall. Because the stress is driven by thermal expansion, its evolution is governed directly by the transient thermal response of the material. As a result, the stress increases as the wall temperature rises and reaches the yield threshold only when the wall has accumulated sufficient thermal energy provided by the combustion system.

In summary, the analyzes presented above show that the thermo-mechanical response of the plane wall remains within the thermoelastic regime only up to the time at which the von Mises stress reaches the temperature-dependent yield strength. Accordingly, all subsequent discussions are carried out up to the time to reach yield strength, beyond which the current thermoelastic framework would no longer be valid.

8.3.1. *Influence of flame strain rate*

In this subsection, we will investigate how the variation of imposed flame strain rate influences the heating process of the plate, with particular emphasis on the time required for the wall to reach its yield strength.

Fig. 12 shows the dependence of the plate's time to reach yield strength on the flame strain rate. A clear trend is observed: this time decreases monotonically as the flame strain rate increases. At first glance, this behavior may appear counter-intuitive. As shown previously in Fig. 8, before the plate is inserted, the flame temperature at the centerline actually decreases with increasing flame strain rate. However, during the transient heating stage, higher flame strain rates lead to a more rapid rise in the wall-surface temperature, resulting in a shorter time for the plate to reach its yield strength. This opposite trend highlights that the governing factor for the thermo-mechanical response is not the eventual flame temperature at the beginning but rather the instantaneous heat transfer rate experienced by the wall.

To better illustrate this mechanism, Fig. 13 presents the temporal evolution of the wall-surface heat flux for different flame strain rates. It is shown clearly that the heat flux through the wall surface is consistently higher when the flame strain rate is larger, starting immediately from the moment the plane wall is inserted into the flame. Consequently, energy is transported from the flame to the plane wall more rapidly throughout the entire heating process, which explains why the wall temperature rises faster and the yield-strength threshold is reached earlier at higher strain rates. The underlying physical mechanism originates from the structural response of the flame to increased strain rate. A larger flame strain rate compresses the reaction zone, making it thinner and shifting it closer to the wall surface. As a result, the local temperature gradient at the wall surface in the flame region ($z = 0^+$) becomes significantly steeper. Since the conductive heat flux is proportional to this gradient, a sharper gradient directly leads to a higher heat flux delivered to the wall. This enhanced near-wall thermal gradient therefore provides the dominant contribution to the accelerated heating observed at higher flame strain rates.

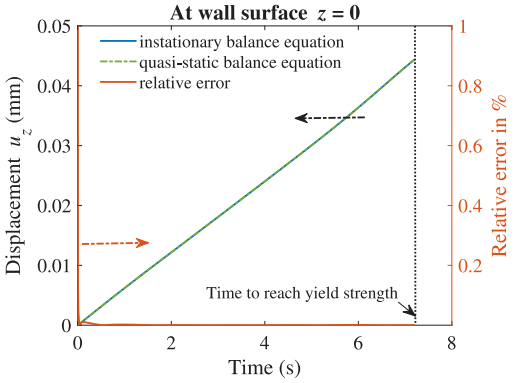

Fig. 14. Time development of the displacement u_z using instationary balance equation of momentum (blue solid line) and quasi-static balance equation (green dashed line), and the corresponding relative error of using quasi-static equation at the position wall surface $z = 0$. Flame strain rate: $a = 500$ 1/s.

8.3.2. *Validity of quasi-static assumption*

To evaluate the validity of the quasi-static assumption, we compare the displacement obtained from the instationary balance equation ($\rho_0 \ddot{\boldsymbol{u}} = \mathrm{div}(\boldsymbol{\sigma})$, without considering of body force), to that obtained using the quasi-static balance equation ($0 = \mathrm{div}(\boldsymbol{\sigma})$). Fig. 14 shows the time evolution of the wall-surface displacement u_z at $z = 0$, computed using the instationary formulation (blue solid line) and the quasi-static formulation (green dashed line). The corresponding relative error between the two solutions is also indicated on the right y-axis. This example uses a flame strain rate of 500 1/s. The curves are shown up to the time at which the flame-induced thermomechanical stress at the wall surface reaches the yield strength.

From the relative-error curve, it is clear that the displacement obtained from the quasi-static equation remains within approximately $\mathcal{O}(10^{-2}\%)$ of the instationary solution for almost the entire time evolution. Therefore, using the quasi-static balance equation to compute the stress and deformation fields in the plane wall during the heating process does not introduce additional error.

It should be noted, however, that during the very early stage immediately after the plane wall is introduced into the flame, the wall-surface temperature increases in a sudden manner. This rapid temperature rise causes a similarly abrupt change in displacement, leading to a relative error of about 1% when using the quasi-static formulation. Despite this short transient deviation, the quasi-static assumption remains valid for the remainder of the heating process.

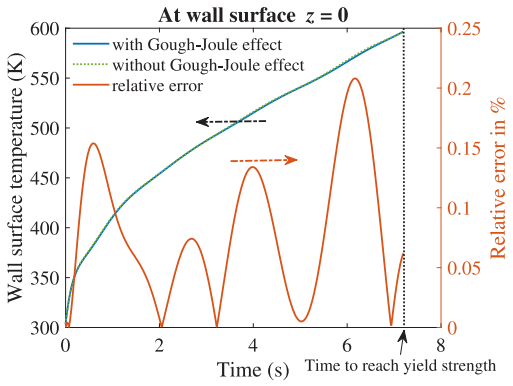

Fig. 15. Time development of the wall surface temperature $T(z = 0)$ with and without term describing Gough-Joule effect, and the corresponding relative error of without consideration of Gough-Joule effect at the position wall surface $z = 0$. Flame strain rate: $a = 500$ 1/s.

8.3.3. *Importance of Gough-Joule effect*

To assess the importance of the Gough–Joule effect during flame-solid interaction, Fig. 15 compares the time evolution of the plane-wall surface temperature (i.e., the maximum temperature within the solid) for simulations performed with and without the Gough–Joule term, namely $-T\boldsymbol{\beta} \cdot \dot{\boldsymbol{\epsilon}}$ in Eq. (10). The right y-axis additionally shows the relative error (in %) introduced when the Gough–Joule effect is neglected.

The results show that the temperature histories obtained from the two simulations are nearly indistinguishable. The maximum relative error remains below approximately 0.2% throughout the entire heating process up to the time when the yield strength is reached. Such a small deviation indicates that, at least for the Inconel 718 plate considered here, the influence of the Gough–Joule term is negligible in comparison with heat conduction, which dominates the temperature rise within the solid. Due to the relatively low thermal diffusivity of the material, the deformation rate induced by the gradual temperature increase is slow, limiting the magnitude of the Gough–Joule contribution.

It should be explicitly noted that, although the Gough–Joule effect is negligible for the heating process considered here, this conclusion does not necessarily extend to other flame–solid interaction scenarios. In processes where the material experiences rapid or large pressure variations, the volumetric strain rate can become significantly higher, and the associated temperature rise caused by the Gough–Joule effect may no longer be negligible. Examples include ignition events involving sharp pressure transients, detonation-to-deflagration transition, or combustion systems in which strong compressive waves impinge on the solid material. In such situations, the mechanical contribution to the temperature field may play a more prominent role, and the importance of the Gough–Joule effect should be re-evaluated. A systematic quantification of this effect under such conditions is considered to be future investigation.

9. Conclusions

In this work, a fully coupled flame–solid interaction problem has been investigated using a laminar strained premixed ammonia/hydrogen/air flame stabilized at a plane wall. Both steady-state and transient heating processes were studied, with particular emphasis on flame-induced heating and the resulting thermo-mechanical response of the solid wall. Heat transfer from the flame to the wall was explicitly accounted for via conjugate heat transfer modeling, allowing the mutual coupling between flame dynamics, heat transfer and solid deformation to be resolved. Inconel 718 was selected as a representative wall material, and its temperature-dependent thermo-physical properties were modeled using thermodynamically consistent formulations derived from the Helmholtz energy. This approach ensured a thermodynamically consistent coupling between the thermal and mechanical fields under strongly transient and spatially non-uniform temperature conditions.

Although direct experimental validation of the fully coupled flame–solid interaction remains challenging due to the lack of detailed measurements, the present model reproduces physically consistent trends in both flame structure and solid response, providing confidence in its predictive capability.

In the steady-state configuration, the influence of thermal radiation on the wall temperature distribution was assessed and shown to be secondary compared to conductive heat transfer for the conditions considered.

For the transient heating process, it was shown that the introduction of a cold plane wall into the flame system can lead either to flame extinction or successful wall heating, depending on the imposed flame strain rate. In the successful heating regime, increasing the flame strain rate was found to accelerate wall heating and significantly reduce the time required for the thermo-mechanical stress to reach the material yield strength, despite the lower flame temperatures associated with higher strain rates. This counter-intuitive behavior was attributed to enhanced heat flux at the flame–wall interface caused by the narrowing and displacement of the reaction zone toward the wall.

Furthermore, the quasi-static assumption used in the balance equation of linear momentum for solid mechanics was validated throughout the heating process up to the onset of yielding, and the Gough–Joule effect was shown to have a negligible influence on the predicted temperature and deformation fields for the material and conditions studied. Overall, the present work provides fundamental insight into transient flame-induced heating and thermo-mechanical stress development in solid structures, with direct relevance to the design and safe operation of combustion systems involving high-temperature materials.

Finally, it should be noted that the present study assumes an inert and non-permeable wall surface, thereby neglecting potential mass transfer effects such as pyrolysis-driven blowing. In many flame spread problems over reactive solids as discussed in [13], such wall-normal transpiration can modify the near-wall flow field, alter the flame position and redistribute the heat flux between convective and diffusive contributions. Considering such effects into the present thermodynamically consistent framework would provide a more comprehensive description of flame–solid interaction and represents a promising direction for future work.

CRediT authorship contribution statement

Chunkan Yu: Writing – original draft, Validation, Software, Resources, Methodology, Investigation, Funding acquisition, Formal analysis, Conceptualization. **Frederik Hille:** Writing – original draft, Validation, Methodology, Formal analysis. **Thomas Böhlke:** Writing – review & editing, Methodology, Conceptualization. **Michael Fischlschweiger:** Writing – review & editing, Validation, Methodology.

Declaration of competing interest

The authors declare the following financial interests/personal relationships which may be considered as potential competing interests: Chunkan Yu reports financial support was provided by German Research Foundation. If there are other authors, they declare that they have no known competing financial interests or personal relationships that could have appeared to influence the work reported in this paper.

Acknowledgments

C.Yu acknowledges financial support by the DFG, Germany (project H2MAT3D, project number 523879740 within the DFG-SPP 2419 HyCAM).

Data availability

Data will be made available on request.

References

[1] R.A. Antunes, M.C.L. de Oliveira, Corrosion in biomass combustion: A materials selection analysis and its interaction with corrosion mechanisms and mitigation strategies, Corros. Sci. 76 (2013) 6–26.

[2] A. Kranzmann, T. Neddemeyer, A.S. Ruhl, D. Hünert, D. Bettge, G. Oder, R.S. Neumann, The challenge in understanding the corrosion mechanisms under oxyfuel combustion conditions, Int. J. Greenh. Gas Control. 5 (2011) S168–S178.

[3] H. Yan, H. Xie, W. Zheng, L. Liu, Numerical simulation of combustion and melting process in an aluminum melting furnace: A study on optimizing stacking mode, Appl. Therm. Eng. 245 (2024) 122840.

[4] E. Dreizin, Phase changes in metal combustion, Prog. Energy Combust. Sci. 26 (1) (2000) 57–78.

[5] J. Nie, J. Liang, H. Zhang, Y. Zou, Q. Jiao, Y. Li, X. Guo, S. Yan, Y. Zhu, Evolution of structural damage of solid composite propellants under slow heating and effect on combustion characteristics, J. Mater. Res. Technol. 25 (2023) 5021–5037.

[6] P. Schulz, D. Dziedzic, N. Rocha, C. Ezenwajiaku, M. Talibi, R. Balachandran, E. Galindo-Nava, Hydrogen uptake and embrittlement in nickel-base superalloys during hydrogen flame charging, Commun. Mater. 6 (1) (2025) 265.

[7] C. Yu, T. Böhlke, A. Valera-Medina, B. Yang, U. Maas, Flame–solid interaction: Thermomechanical analysis for a steady laminar stagnation flow stoichiometric NH3–H2 flame at a plane wall, Energy Fuels 37 (4) (2023) 3294–3306.

[8] M. Schneider, H. Nicolai, V. Schuh, M. Steinhausen, C. Hasse, Flame-wall interaction of thermodiffusively unstable hydrogen/air flames, Part I: Characterization of governing physical phenomena, Combust. Flame 279 (2025) 114320.

[9] A.W.A. Al-Fatlawi, M.A.S. Al-Baghdadi, M. Al-Waily, Thermal stress analysis of a reactor used to produce hydrogen from hydrocarbon fuel, Int. J. Hydrog. Energy 50 (2024) 605–613.

[10] A.K. Pozarlik, J.B. Kok, Fluid-structure interaction in combustion system of a gas turbine—effect of liner vibrations, J. Eng. Gas Turbines Power 136 (9) (2014) 091502.

[11] E. Stefan, B. Talic, Y. Larring, A. Gruber, T.A. Peters, Materials challenges in hydrogen-fuelled gas turbines, Int. Mater. Rev. 67 (5) (2022) 461–486.

[12] E. Bakan, D.E. Mack, G. Mauer, R. Vaßen, J. Lamon, N.P. Padture, High-temperature materials for power generation in gas turbines, in: Advanced Ceramics for Energy Conversion and Storage, Elsevier, 2020, pp. 3–62.

[13] Y. Ma, S. Tao, Z. Guo, Y. Gu, Z. Zhao, Z. Li, S. Ding, S.H. Chung, O. Fujita, L. Hu, Flame spread over solid materials under reduced buoyancy/gravity, Prog. Energy Combust. Sci. 111 (2025) 101251.

[14] J. Lemaitre, J.-L. Chaboche, Mechanics of Solid Materials, Cambridge University Press, Cambridge, UK, 1994.

[15] A. Prahs, T. Böhlke, On invariance properties of an extended energy balance, Contin. Mech. Thermodyn. 32 (3) (2020) 843–859.

[16] A. Prahs, M. Reder, D. Schneider, B. Nestler, Thermomechanically coupled theory in the context of the multiphase-field method, Int. J. Mech. Sci. 257 (2023) 108484.

[17] L. Oestringer, C. Proppe, On the fully coupled quasi-static equations for the thermoelastic halfspace, Mech. Mater. 177 (2023) 104554.

[18] E. Stein, R. De Borst, T.J. Hughes, Encyclopedia of Computational Mechanics, Wiley, 2004.

[19] J. Pina, A. Costa, J. Appleton, Formal solution of quasi-static problems, Int. J. Non-Linear Mech. 45 (5) (2010) 525–534.

[20] J. Sanchez, H. Schreyer, D. Sulsky, P. Wallstedt, Solving quasi-static equations with the material-point method, Internat. J. Numer. Methods Engrg. 103 (1) (2015) 60–78.

[21] E. Hosseini, V.A. Popovich, A review of mechanical properties of additively manufactured inconel 718, Addit. Manuf. 30 (2019) 100877.

[22] S.P. Kumar, S. Elangovan, R. Mohanraj, J. Ramakrishna, A review on properties of inconel 625 and inconel 718 fabricated using direct energy deposition, Mater. Today: Proc. 46 (2021) 7892–7906.

[23] M.A. Kattimani, P. Venkatesh, L. Kirthan, M.M. Math, A. Prapul Chandra, R. Hegde, C.D. Prasad, M. Gupta, S. Kumar, Design and optimization of fatigue life studies on induction hardened IN718 alloy for gas turbine applications, Adv. Mater. Process. Technol. 10 (4) (2024) 3607–3619.

[24] A. Valera-Medina, H. Xiao, M. Owen-Jones, W.I. David, P.J. Bowen, Ammonia for power, Prog. Energy Combust. Sci. 69 (2018) 63–102.

[25] C.W. Ong, N. Chang, M.-L. Tsai, C.-L. Chen, Decarbonizing the energy supply chain: Ammonia as an energy carrier for renewable power systems, Fuel 360 (2024) 130627.

[26] Y. Liu, M. Luo, W. Li, C. Zhou, X. Huo, Z. Pan, R. Chen, L. An, Techno-economic analysis of using ammonia as an energy carrier for renewable energy conversion and storage, Int. J. Hydrog. Energy 162 (2025) 150784.

[27] J. Li, H. Huang, L. Deng, Z. He, Y. Osaka, N. Kobayashi, Effect of hydrogen addition on combustion and heat release characteristics of ammonia flame, Energy 175 (2019) 604–617.

[28] R. Khamedov, W. Song, F.E. Hernandez-Perez, H.G. Im, Heat release characteristics of ammonia flames in MILD conditions, Fuel 354 (2023) 129138.

[29] A. Goldmann, F. Dinkelacker, Investigation of boundary layer flashback for non-swirling premixed hydrogen/ammonia/nitrogen/oxygen/air flames, Combust. Flame 238 (2022) 111927.

[30] A. Adam, A. Abdulnaim, R. Kai, H. Watanabe, Differential diffusion effect on NH3/H2 non-premixed turbulent flame structure and chemical kinetics, Int. J. Hydrog. Energy 102 (2025) 20–28.

[31] X. Chen, T. Guivarch, H. Lulic, C. Hasse, Z. Chen, F. Ferraro, A. Scholtissek, Evaluation of hydrogen/ammonia substitute fuel mixtures for methane: effect of differential diffusion, Int. J. Hydrog. Energy 69 (2024) 1056–1068.

[32] M.E. Gurtin, E. Fried, L. Anand, The Mechanics and Thermodynamics of Continua, Cambridge University Press, 2010.

[33] P. Haupt, Continuum Mechanics and Theory of Materials, Springer Berlin, Heidelberg, 2002.

[34] B.D. Coleman, W. Noll, The thermodynamics of elastic materials with heat conduction and viscosity, Arch. Ration. Mech. Anal. 13 (1963) 167–178.

[35] K. Wilmanski, Thermomechanics of Continua, Springer Berlin Heidelberg, Heidelberg, 2012.

[36] U. Maas, J. Warnatz, Ignition processes in hydrogen- oxygen mixtures, Combust. Flame 74 (1) (1988) 53–69.

[37] T. Szabó, J. Yáñez, A. Kotchourko, M. Kuznetsov, T. Jordan, Parameterization of laminar burning velocity dependence on pressure and temperature in hydrogen/air/steam mixtures, Combust. Sci. Technol. 184 (10–11) (2012) 1427–1444.

[38] V. Giurcan, M. Mitu, D. Razus, D. Oancea, Experimental study and kinetic modeling of laminar flame propagation in premixed stoichiometric n-butane-air mixture, Rev. Chim 70 (2019) 1125–1131.

[39] S. Eckart, C. Yu, U. Maas, H. Krause, Experimental and numerical investigations on extinction strain rates in non-premixed counterflow methane and propane flames in an oxygen reduced environment, Fuel 298 (2021) 120781.

[40] C. Strassacker, V. Bykov, U. Maas, REDIM reduced modeling of quenching at a cold wall including heterogeneous wall reactions, Int. J. Heat Fluid Flow 69 (2018) 185–193.

[41] G. Stahl, J. Warnatz, Numerical investigation of time-dependent properties and extinction of strained methane- and propane-air flamelets, Combust. Flame 85 (3–4) (1991) 285–299.

[42] J.O. Hirschfelder, C.F. Curtiss, R.B. Bird, M.G. Mayer, Molecular Theory of Gases and Liquids, vol. 165, Wiley New York, 1964.

[43] L.S. Rothman, I.E. Gordon, A. Barbe, D.C. Benner, P.F. Bernath, M. Birk, V. Boudon, L.R. Brown, A. Campargue, J.-P. Champion, et al., The HITRAN 2008 molecular spectroscopic database, J. Quant. Spectrosc. Radiat. Transfer 110 (9–10) (2009) 533–572.

[44] H. Nakamura, M. Shindo, Effects of radiation heat loss on laminar premixed ammonia/air flames, Proc. Combust. Inst. 37 (2) (2019) 1741–1748.

[45] J. Jian, H. Hashemi, H. Wu, P. Glarborg, A.W. Jasper, S.J. Klippenstein, An experimental, theoretical, and kinetic modeling study of post-flame oxidation of ammonia, Combust. Flame 261 (2024) 113325.

[46] C.A. Petrov, A.F. Ghoniem, The transient response of strained laminar-premixed flames, Combust. Flame 102 (3) (1995) 401–417.

[47] D.-H. Kim, J.-H. Kim, J.-W. Sa, Y.-S. Lee, C.-K. Park, S.-I. Moon, Stress rupture characteristics of inconel 718 alloy for ramjet combustor, Mater. Sci. Eng.: A 483 (2008) 262–265.

[48] J. Díaz-Álvarez, J. Cantero, H. Miguélez, X. Soldani, Numerical analysis of thermomechanical phenomena influencing tool wear in finishing turning of inconel 718, Int. J. Mech. Sci. 82 (2014) 161–169.

[49] SPACEMATDB – space materials database, 2025, https://www.spacematdb.com/spacemat/manudatasheets/inconel%20718.pdf. (Accessed 28 November 2025).

[50] S.M. Walley, The effect of temperature gradients on elastic wave propagation in split hopkinson pressure bars, J. Dyn. Behav. Mater. 6 (3) (2020) 278–286.

[51] B.M. Marques, C.M. Andrade, D.M. Neto, M.C. Oliveira, J.L. Alves, L.F. Menezes, Numerical analysis of residual stresses in parts produced by selective laser melting process, Procedia Manuf. 47 (2020) 1170–1177.

[52] P. Aba-Perea, T. Pirling, P. Withers, J. Kelleher, S. Kabra, M. Preuss, Determination of the high temperature elastic properties and diffraction elastic constants of Ni-base superalloys, Mater. Des. 89 (2016) 856–863.

[53] Special Metals, 2025, https://www.specialmetals.com/documents/technical-bulletins/inconel/inconel-alloy-718.pdf. (Accessed 28 November 2025).

[54] L. Yule, N. Harris, M. Hill, B. Zaghari, Temperature monitoring of through-thickness temperature gradients in thermal barrier coatings using ultrasonic guided waves, J. Nondestruct. Eval. 43 (1) (2024) 22.

[55] D.R. Gaskell, D.E. Laughlin, Introduction to the Thermodynamics of Materials, CRC Press, Boca Raton, USA, 2024.

[56] I. Hernando, M.A. Renderos, M. Cortina, J.E. Ruiz, J.I. Arrizubieta, A. Lamikiz, Inconel 718 laser welding simulation tool based on a moving heat source and phase change, Procedia CIRP 74 (2018) 674–678.

[57] D. Basak, R. Overfelt, D. Wang, Measurement of specific heat capacity and electrical resistivity of industrial alloys using pulse heating techniques, Int. J. Thermophys. 24 (6) (2003) 1721–1733.

[58] A.S. Agazhanov, D. Samoshkin, Y.M. Kozlovskii, Thermophysical properties of inconel 718 alloy, in: Journal of Physics: Conference Series, vol. 1382, (1) IOP Publishing, 2019.
[59] Y. Zhang, T.T. Zuo, Z. Tang, M.C. Gao, K.A. Dahmen, P.K. Liaw, Z.P. Lu, Microstructures and properties of high-entropy alloys, Prog. Mater. Sci. 61 (2014) 1–93.
[60] C. Yu, S. Srikanth, T. Böhlke, B. Gorr, U. Maas, Steady laminar stagnation flow NH3-H2-air flame at a plane wall: Flame extinction limit and its influence on the thermo-mechanical stress and corrosive behavior of wall materials, Appl. Energy Combust. Sci. 18 (2024) 100261.
[61] C. Sung, J. Liu, C.K. Law, Structural response of counterflow diffusion flames to strain rate variations, Combust. Flame 102 (4) (1995) 481–492.
[62] C.K. Law, C. Sung, G. Yu, R. Axelbaum, On the structural sensitivity of purely strained planar premixed flames to strain rate variations, Combust. Flame 98 (1–2) (1994) 139–154.
[63] F.N. Egolfopoulos, Dynamics and structure of unsteady, strained, laminar premixed flames, in: Symposium (International) on Combustion, vol. 25, (1) Elsevier, 1994, pp. 1365–1373.